THE JOURNAL OF PHYSICAL CHEMISTRY C

Article

pubs.acs.org/JPCC

Synthesis of Magnetically Separable and Recyclable g-C_3N_4–Fe_3O_4 Hybrid Nanocomposites with Enhanced Photocatalytic Performance under Visible-Light Irradiation

Santosh Kumar,[†] Surendar T,[†] Bharat Kumar,[‡] Arabinda Baruah,[‡] and Vishnu Shanker*,[†]

[†]Department of Chemistry, National Institute of Technology Warangal, Warangal-506004, A.P., India

[‡]Department of Chemistry, Indian Institute of Technology Delhi, New Delhi-110016, India

Supporting Information

ABSTRACT: Herein we demonstrate a facile, reproducible, and template-free strategy to prepare g-C_3N_4–Fe_3O_4 nanocomposites by an in situ growth mechanism. The results indicate that monodisperse Fe_3O_4 nanoparticles with diameters as small as 8 nm are uniformly deposited on g-C_3N_4 sheets, and as a result, aggregation of the Fe_3O_4 nanoparticles is effectively prevented. The as-prepared g-C_3N_4–Fe_3O_4 nanocomposites exhibit significantly enhanced photocatalytic activity for the degradation of rhodamine B under visible-light irradiation. Interestingly, the g-C_3N_4–Fe_3O_4 nanocomposites showed good recyclability without loss of apparent photocatalytic activity even after six cycles, and more importantly, g-C_3N_4–Fe_3O_4 could be recovered magnetically. The high performance of the g-C_3N_4–Fe_3O_4 photocatalysts is due to a synergistic effect including the large surface-exposure area, high visible-light-absorption efficiency, and enhanced charge-separation properties. In addition, the superparamagnetic behavior of the as-prepared g-C_3N_4–Fe_3O_4 nanocomposites also makes them promising candidates for applications in the fields of lithium storage capacity and bionanotechnology.

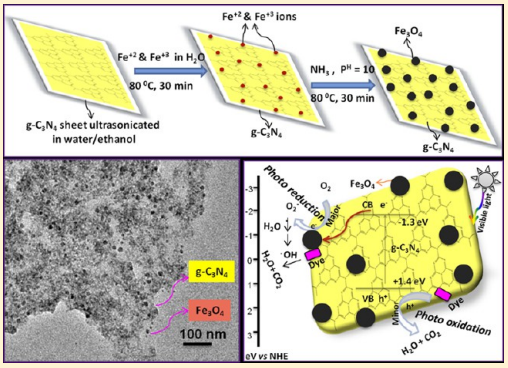

INTRODUCTION

Semiconductor photocatalysis has emerged as a most promising new technology in the past few years for the production of clean energy and environmental remediation because the use of catalysts and solar energy is most economical.[1−3] A significantly efficient, stable, inexpensive, easily separable semiconductor material that is capable of light harvesting is also essential for an economical use of catalysts.[4] Therefore, intense research activity has recently been focused on the development of an efficient semiconductor material with unique properties apart from TiO_2, which can directly split water or degrade environmental pollutants using solar energy.[4−8] More recently, graphitic carbon nitride (g-C_3N_4) was found to be a typical metal-free polymeric semiconductor material with a suitable band gap to absorb visible-light radiation and unique properties.[9] Therefore, it is promising to consider graphitic carbon nitride as an alternative candidate for solar light harvesting and conversion because of its many interesting features, including visible-light adsorption ability and ease of large-scale preparation, which is always preferred for practical applications. Also, chemical functionalization or doping of g-C_3N_4 is easy because of its intrinsic organic nature, thus allowing its electronic band gap structure to be tuned, and contrary to many other organic semiconductors, graphitic carbon nitride has high thermal and chemical stability against oxidation reactions and is stable in atmosphere up to 500 °C.[10−14] To date, a large number of articles concerning the synthesis of g-C_3N_4 and its derivatives have been published. For example, loading some cocatalysts onto the surface of the catalyst and doping g-C_3N_4 with nonmetals such as B, C, and S can evidently promote the separation efficiency of photo-induced electron–hole pairs.[15−18] Another feasible strategy to improve its photocatalytic performance is to form a composite with a metal or another semiconductor by designing an appropriate textural porosity.[12,14,19−22] Unfortunately, the performance of the present g-C_3N_4-based photocatalysts does not meet the needs of practical applications because of the inconvenience of recycling these catalysts due to their highly dispersive nature, the fact that conventional separation techniques may lead to loss of catalyst, and the lack of a facile and environmentally friendly strategy to prepare g-C_3N_4-based photocatalysts with desired properties. Therefore, the development of a highly effective visible-light-driven photocatalyst for the production of clean energy and environmental remediation is still being sought.

On the other hand, Fe_3O_4 nanoparticles have attracted much interest because of their magnetic properties, which have led to their applications in drug delivery systems,[23,24] lithium storage capacity,[25] wastewater treatment,[26] magnetic resonance imaging,[27,28] and protein separation.[29] Interestingly, Fe_3O_4 can be

Received: October 1, 2013
Revised: November 16, 2013
Published: November 20, 2013

considered as a conductor because its conductivity is as high as 1.9×10^6 S m^{-1}, which is different from the other semiconductor characteristics of most metal oxide materials.[30] Heterostructured catalysts composed of magnetic components, including metal/Fe_3O_4, graphene/Fe_3O_4, WO_3/Fe_3O_4, and TiO_2/Fe_3O_4, have shown improved performance due to their unique properties and potential applications that could not be achieved solely with a single-component catalyst.[27−33] In this context, these studies initially intended to integrate superparamagnetic iron oxide nanoparticles and g-C_3N_4 sheets into a single hybrid nanocomposite as an efficient visible-light photocatalyst because the high conductivity of Fe_3O_4 and energy band structure matching (E_{CB} = 1 V vs NHE) makes it a good candidate for coupling with g-C_3N_4 and improving the photocatalytic performance by enhancing the photoinduced charge separation of electron−hole pairs and transport.

In this present work, we have developed a facile and reproducible strategy for preparing g-C_3N_4−Fe_3O_4 hybrid nanocomposites. The as-prepared nanocomposites were structurally characterized by X-ray diffraction (XRD), thermogravimetric analysis/differential thermal analysis (TGA/DTA), FTIR spectroscopy, transmission electron microscopy (TEM), UV−vis diffuse reflectance spectroscopy (DRS), X-ray photoelectron spectroscopy (XPS), and fluorescence spectroscopy. The results demonstrated that successful deposition of uniform monodispersed Fe_3O_4 nanoparticles onto the surface of g-C_3N_4 sheets allows the diffusion of light by multiple pathways to enhance light harvesting, and significantly enhanced photocatalytic activity was observed under visible-light irradiation. A possible mechanism for the enhancement of photocatalytic activity was also investigated. In addition, deposition of magnetic nanoparticles onto the surface of the photocatalysts proved to be an effective way to separate photocatalyst easily from the photocatalytic system with an external magnetic field, allowing them to be reused in multiple cycles. This approach prevented the agglomeration of the catalyst particles during recovery and can increase the durability of the catalysts. Therefore, the goal of the present work was to design more efficient g-C_3N_4-based photocatalysts by recycling and expanding the light absorption further into the visible range while still keeping a sufficient overpotential to carry out the desired reactions, making Fe_3O_4 a valuable photocatalytic material for its potential applications in environmental protection.

2. EXPERIMENTAL DETAILS

2.1. Materials. Melamine (Aldrich, 99.0%), ferric chloride (Aldrich, 10% w/v; 99.9% metal-based), ferrous chloride (Aldrich, 99.0%), NH_3 solution (Merck, 25%), and rhodamine B (Aldrich, 85.0%) were used as received. All other reagents used in this work were analytically pure and used without further purification.

2.2. Method. The g-C_3N_4 was prepared by direct heating of melamine to 550 °C for 2 h in a N_2 atmosphere.[19] The g-C_3N_4−Fe_3O_4 nanocomposites were prepared by an in situ precipitation method (Figure S1 in the Supporting Information). In a typical procedure, g-C_3N_4 (125 mg) was dispersed in 500 mL of ethanol/water (1:2) and ultrasonicated (PCI Analytics, 12 mm probe, 33 Hz, 150 W) for 5 h at ambient temperature. $FeCl_3 \cdot 6H_2O$ (1.838 g, 0.0216 mol) and $FeCl_2 \cdot 4H_2O$ (0.703 g, 0.0108 mol) were dissolved separately in 20 mL of double-distilled water and added to the suspension of g-C_3N_4. The mixture was stirred at 80 °C for 30 min, and then 10 mL of ammonia solution (NH_4OH) was quickly injected into the reaction mixture. The resulting mixture was stirred for another 30 min, after which the reaction mixture was cooled and washed several times with double-distilled water and absolute alcohol. Finally, the as-obtained precipitate was dried in air at 80 °C for further characterization. For comparison, free Fe_3O_4 nanoparticles were also synthesized using exactly the same procedure without adding g-C_3N_4. The as-prepared g-C_3N_4−Fe_3O_4 photocatalysts with 7.5, 15.2, and 23.0 wt % Fe_3O_4 were named as CNFO-7.5, CNFO-15.2, and CNNFO-23.0, respectively. The pure g-C_3N_4 was named as CN, and Fe_3O_4 was named as FO.

2.3. Characterization. XRD studies were carried out on a Bruker D8 Advance diffractometer using Ni-filtered Cu Kα radiation. TGA/DTA experiments were carried out on PerkinElmer Pyris Diamond TGA/DTA system on well-ground samples in an air atmosphere at a heating rate of 10 °C min^{-1}. The FTIR spectra were recorded in transmission mode from 4000 to 400 cm^{-1} on a Nicolate Protégé 460 FTIR spectrometer using KBr discs. TEM was done on a JEOL JSM-6700F instrument. UV−vis DRS spectra were recorded on a PerkinElmer Lambda 20 UV−vis−NIR spectrophotometer equipped with an integrating sphere to record the diffuse reflectance spectra of the samples, and $BaSO_4$ was used as a reference. Nitrogen adsorption−desorption isotherms were measured using a Quantachrome NOVA 1200e analyzer. Chemical compositions of the samples were analyzed by XPS (Kratos Axis ULTRA system incorporating a 165 mm hemispherical electron energy analyzer). The photoluminescence (PL) spectra of photocatalysts were recorded on a TSC Solutions F96PRO fluorescence spectrophotometer at an excitation wavelength of 365 nm.

2.4. Photocatalytic Activity. Rhodamine B (RhB), a widely used dye, was chosen as a model pollutant to examine the visible-light-driven photocatalytic activity of the samples. The photocatalytic activity of the samples was evaluated via degradation of RhB in an aqueous solution under visible-light irradiation. The visible-light source was a solar simulator 300 W Xe lamp (Asahi Spectra Co., Ltd.). The photocatalyst (0.025 g) was added to an aqueous solution of RhB (100 mL, 5 mg L^{-1}) in a beaker at room temperature under stirring at 250 rpm throughout the test under visible-light irradiation. Prior to irradiation, the solution was stirred continuously for 30 min in the dark to establish an adsorption−desorption equilibrium. During photocatalytic processes, the sample was periodically withdrawn, centrifuged to separate the photocatalyst from the solution, and used for the absorbance measurement. The concentration of RhB during the degradation process was monitored using a UV−Vis spectrophotometer.

2.5. Detection of Reactive Species. The detection process for reactive oxidative species was similar to the experimental photodegradation process. Various scavengers were added to the RhB solution prior to addition of the photocatalyst. Furthermore, the PL spectrum with terephthalic acid (TA) as a probe molecule was used to disclose the formation of $^{\bullet}OH$ radicals on the surface of g-C_3N_4 under visible-light irradiation. In a brief experimental procedure, photocatalyst (0.1 g) was dispersed in 40 mL of an aqueous solution of TA (5×10^{-4} mol L^{-1}) and NaOH (2×10^{-3} mol L^{-1}) at room temperature. The above suspension was subjected to the photocatalytic activity evaluation of the photocatalyst under visible-light irradiation, and the PL intensity was measured using a fluorescence spectrophotometer at an excitation wavelength of 365 nm.

Scheme 1. Schematic Representation of the in Situ Deposition of Fe_3O_4 Nanoparticles on a g-C_3N_4 Sheet

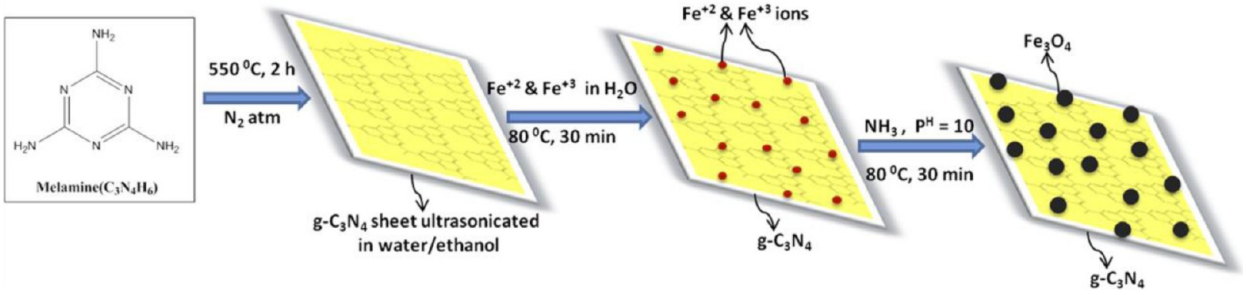

2.6. Electrochemical Impedance Spectroscopy (EIS). EIS measurements were performed on an IM6e electrochemical workstation (ZAHNER Electrik, Kronach, Germany) based on a conventional three-electrode system consisting of carbon paste as the working electrode, a platinum wire as the counter electrode, and Ag/AgCl (3 N KCl) as the reference electrode. The EIS measurements were performed in a 0.1 mol L^{-1} $NaSO_4$ solution containing 5 mmol L^{-1} $[Fe(CN)_6]^{3-}$/$[Fe(CN)_6]^{4-}$ over the frequency range from 0.01 Hz to 100 kHz at 0.24 V, and the amplitude of the applied sine wave potential in each case was 5 mV.

3. RESULTS AND DISCUSSION

3.1. Formation of g-C_3N_4–Fe_3O_4 Nanocomposites. The in situ growth mechanism has been widely employed to synthesize a variety of carbon-based composites.[19,23,29] A similar strategy was used for the preparation of the g-C_3N_4–Fe_3O_4 hybrid nanocomposites, as shown in Scheme 1. When iron salts were mixed with ultrasonically dispersed g-C_3N_4 sheets, the iron ions were deposited on the surface of g-C_3N_4 via chemical adsorption. Furthermore, iron ions were converted into Fe_3O_4 nanoparticles with controlled growth by using ammonia as a precipitating agent at room temperature. Thus, finely distributed and uniform Fe_3O_4 nanoparticles were successfully deposited on the surface of the g-C_3N_4 sheets. To minimize the surface energy, the as-prepared Fe_3O_4 nanoparticles led the heterojunction at the interface of the g-C_3N_4 and Fe_3O_4 in the resulting composite system. The size of the Fe_3O_4 nanoparticles in the hybrid nanocomposite was as small as 8 nm. The in situ growth mechanism also avoided the agglomeration of Fe_3O_4 nanoparticles.

3.2. Catalyst Characterization. To calculate the content of Fe_3O_4 nanoparticles on g-C_3N_4 sheets, TGA was performed on g-C_3N_4–Fe_3O_4 nanocomposites under an air atmosphere from 50 to 800 °C. As can be seen from Figure 1, the decomposition of g-C_3N_4 starts at 550 °C and is completed at ~720 °C, which is attributed to the burning of g-C_3N_4.[9] This weight loss region could be seen in the g-C_3N_4–Fe_3O_4 hybrid composite samples. The residual weight fractions of the different nanocomposites (CNFO-7.5, CNFO-15.2, and CNNFO-23.0) were found to be 7.5, 15.2, and 23.0%, which are considered to be the contents of Fe_3O_4 in the g-C_3N_4–Fe_3O_4 nanocomposites.

Figure 2 shows the XRD patterns of pure Fe_3O_4, pure g-C_3N_4, and the hybrid composites CNFO-7.5, CNFO-15.2, and CNFO-23.0, which were used to elucidate the phase and structural parameters. The observed diffraction peaks of pure Fe_3O_4 are in good agreement with those reported in the literature for pure face-centered-cubic Fe_3O_4.[23,26] For g-C_3N_4, a strong peak at 2θ = 27.5° corresponding to the characteristic

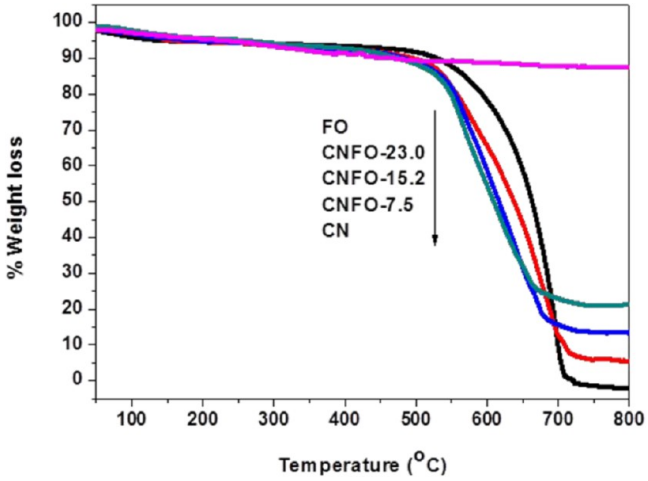

Figure 1. TGA curves of pure g-C_3N_4, pure Fe_3O_4, and the as-prepared g-C_3N_4–Fe_3O_4 photocatalysts.

interplanar stacking peak (002) of an aromatic system was observed.[9] The diffraction peak (002) is a characteristic peak of g-C_3N_4 that was also present in pattern of the g-C_3N_4–Fe_3O_4 nanocomposite. It was also seen that the crystal phase of Fe_3O_4 did not change after hybridization with g-C_3N_4, but the diffraction peak positions for Fe_3O_4 were located at slightly lower angles than those for pure Fe_3O_4, suggesting a strong interaction between Fe_3O_4 and g-C_3N_4. Moreover, no other impurity phase was seen, indicating the g-C_3N_4–Fe_3O_4 to be a two-phase composite.

Figure 3 shows the FTIR spectra of pure Fe_3O_4, pure g-C_3N_4, and the g-C_3N_4–Fe_3O_4 hybrid nanocomposites. The broad Fe–O band in the region from 550 to 650 cm^{-1} is clearly visible at all compositions.[28] In the FTIR spectrum of g-C_3N_4, the broad band around 3100 cm^{-1} is indicative of the N–H stretching vibration, and the peaks at 1243 and 1637 cm^{-1} correspond to C–N and C═N stretching vibrations, respectively. The peak at 808 cm^{-1} is related to the s-triazine ring vibrations.[9,19] The characteristic peaks of g-C_3N_4 and Fe_3O_4 are retained in the g-C_3N_4–Fe_3O_4 hybrid nanocomposite samples. However, a broad band around 3300–3600 cm^{-1} and a band at 1658 cm^{-1} are observed, corresponding to OH stretching vibrations of adsorbed water molecules, and another peak at 1384 cm^{-1} corresponds to the H–O–H bending band of the adsorbed H_2O molecules on the surface of the products. The IR bands due to adsorbed water arise from water released as a decomposition product that later gets adsorbed during the measurement.

Figure 4 shows the UV–vis DRS spectra of pure Fe_3O_4, pure g-C_3N_4, and the g-C_3N_4–Fe_3O_4 hybrid nanocomposite

dx.doi.org/10.1021/jp409651g | J. Phys. Chem. C 2013, 117, 26135–26143

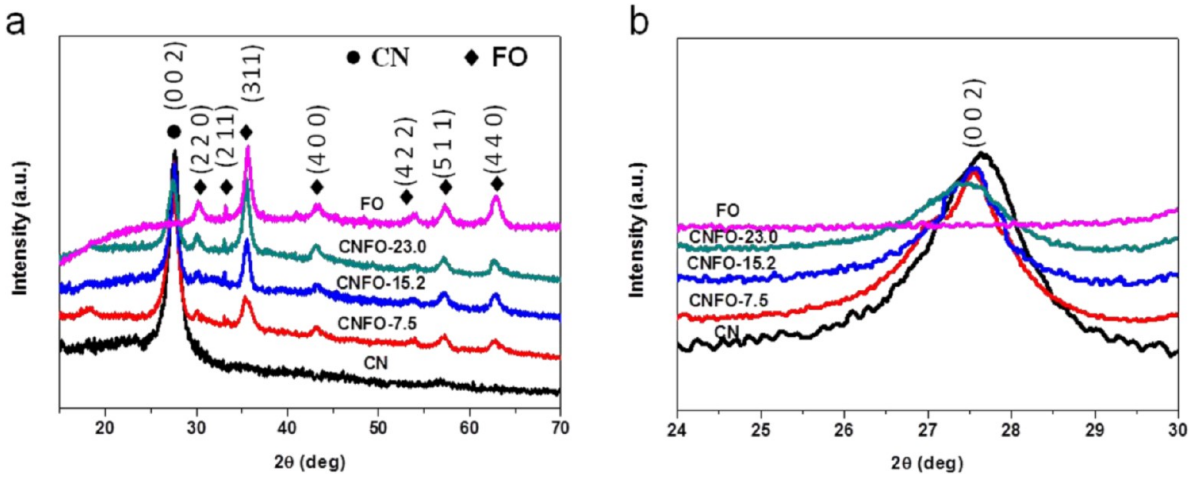

Figure 2. XRD patterns of pure g-C_3N_4, pure Fe_3O_4, and the as-prepared g-C_3N_4–Fe_3O_4 photocatalysts.

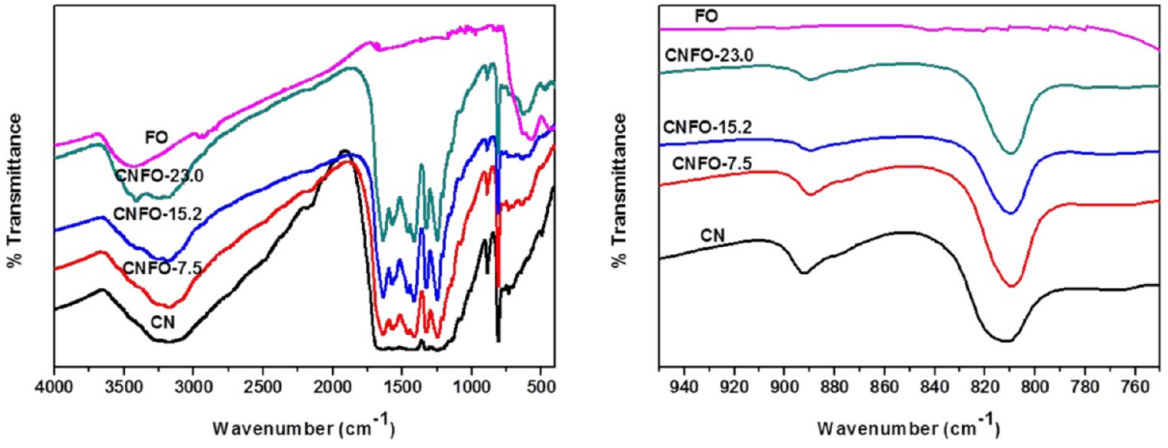

Figure 3. FTIR spectra of pure g-C_3N_4, pure Fe_3O_4, and the as-prepared g-C_3N_4–Fe_3O_4 photocatalysts.

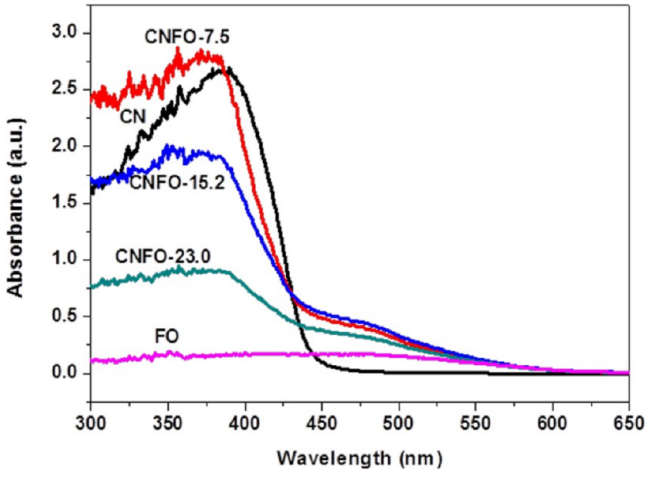

Figure 4. UV–vis DRS spectra of pure g-C_3N_4, pure Fe_3O_4, and the as-prepared g-C_3N_4–Fe_3O_4 photocatalysts.

samples. The pure g-C_3N_4 sample showed an adsorption edge of 450 nm, corresponding to a band gap of 2.76 eV, which signifies its photocatalytic activity under visible-light irradiation. The absorption of the g-C_3N_4–Fe_3O_4 nanocomposites within the visible-light range significantly increased, and a red shift in comparison with the pure g-C_3N_4 appeared. These results are attributed to the interaction between the g-C_3N_4 sheet and the Fe_3O_4 nanoparticles in the composite system. The enhanced light absorption of the g-C_3N_4–Fe_3O_4 nanocomposite led to the generation of more photoinduced electron–hole pairs under visible-light irradiation, which subsequently resulted in enhanced photocatalytic activity.

Figure 5 shows TEM images of pure Fe_3O_4 and pure g-C_3N_4 samples. The pure g-C_3N_4 consists of a sheet structure (Figure 5a), whereas the pure Fe_3O_4 nanoparticles have sizes ranging from 50 to 200 nm (Figure 5b). No distinctive morphological features appeared for Fe_3O_4 nanoparticles, and they were highly agglomerated. Figure 6 shows TEM and high-resolution TEM (HRTEM) images of g-C_3N_4–Fe_3O_4 hybrid nanocomposites. The TEM image (Figure 6a) reveals that Fe_3O_4 nanoparticles

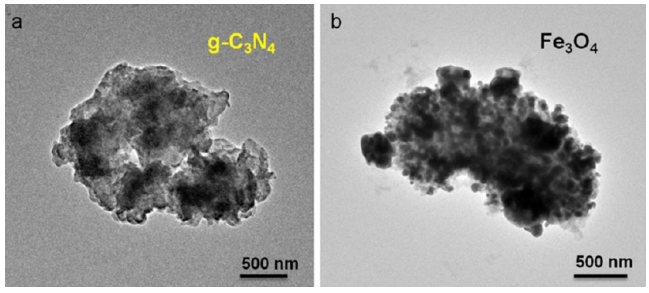

Figure 5. TEM images of (a) pure g-C_3N_4 and (b) pure Fe_3O_4.

dx.doi.org/10.1021/jp409651g | J. Phys. Chem. C 2013, 117, 26135–26143

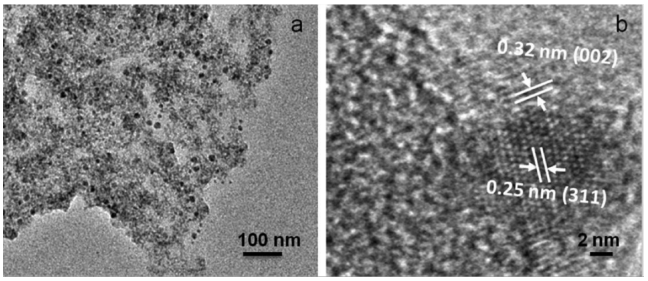

Figure 6. Magnified (a) TEM and (b) HRTEM images of the as-prepared g-C_3N_4–Fe_3O_4 photocatalyst.

were successfully deposited on the surface of the g-C_3N_4 sheet by the in situ growth mechanism; almost no free Fe_3O_4 nanoparticles were found outside of the g-C_3N_4 sheet, which also prevented the agglomeration of Fe_3O_4 nanoparticles. The size of the Fe_3O_4 nanoparticles was found to be around 8 nm. The HRTEM image (Figure 6b) confirms the heterostructure in the g-C_3N_4–Fe_3O_4 nanocomposite system, where the g-C_3N_4 sheet could serve as a support and surfactant to bind with Fe_3O_4 nanoparticles in the resulting composite system. As the content of Fe_3O_4 nanoparticles on the surface of g-C_3N_4 sheet increased from 7.5 to 15.2 wt %, the density of Fe_3O_4 nanoparticles on the surface of g-C_3N_4 sheet increased (Figure S2 in the Supporting Information). Both the UV–vis DRS spectra and TEM results for the g-C_3N_4–Fe_3O_4 nanocomposites suggested the effective assembly of Fe_3O_4 nanoparticles on g-C_3N_4 sheets.

N_2 adsorption–desorption measurements were performed to investigate the Brunauer–Emmett–Teller (BET) specific surface area of pure g-C_3N_4, pure Fe_3O_4, and as-prepared CNFO-15.2. As can be seen from Figure 7a–c, the BET surface area of CNFO-15.2 was found to be 72.73 $m^2\ g^{-1}$, which is much higher than the values for g-C_3N_4 (8.56 $m^2\ g^{-1}$) and bare Fe_3O_4 (6.81 $m^2\ g^{-1}$). Importantly, along with the apparent increment in surface area, an increase in the pore volume from 0.11 $cm^3\ g^{-1}$ for as-prepared g-C_3N_4 to 0.25 $cm^3\ g^{-1}$ for CNFO-15.2 was observed, which facilitated charge separation in the composite system.

To investigate the chemical composition of the CNFO-15.2 composite, XPS measurements were carried out in the region from 0 to 1200 eV. The survey XPS spectrum of CNFO-15.2 shows the coexistence of elements C, N, Fe, and O in the sample (Figure 7d). The Fe 2p XPS spectrum of the CNFO-15.2 composite shows two peaks at 710.0 and 724.1 eV, corresponding to the Fe $2p_{3/2}$ and Fe $2p_{1/2}$ spin–orbit peaks of Fe_3O_4, respectively (Figure 7d inset).[23,25] The peak at 532.7 eV is attributed to O 1s, which belongs to the lattice oxygen of Fe_3O_4. The predominant peaks at 284.5 and 398.2 eV correspond to the C 1s and N 1s of g-C_3N_4, respectively.

3.3. Photocatalytic Activity. The photocatalytic activity of the as-prepared nanocomposites for the degradation of RhB under visible-light irradiation was evaluated (Figure 8). The initial concentration of the RhB suspension was measured and used as the initial concentration C_0. The Y axis is reported as C/C_0, where C is the actual concentration of RhB at the indicated reaction time. As can be clearly seen in Figure 8a, the decrease in the concentration of RhB is faster and more prominent with g-C_3N_4–Fe_3O_4 nanocomposites than with pure g-C_3N_4 or Fe_3O_4 under the same experimental conditions. Without the presence of a catalyst, the degradation of RhB was negligible under visible-light irradiation, indicating the high stability of RhB under visible-light irradiation. To disclose the adsorption effect of the catalyst on RhB, the suspension was stirred for 30 min in the dark to achieve adsorption/desorption equilibration

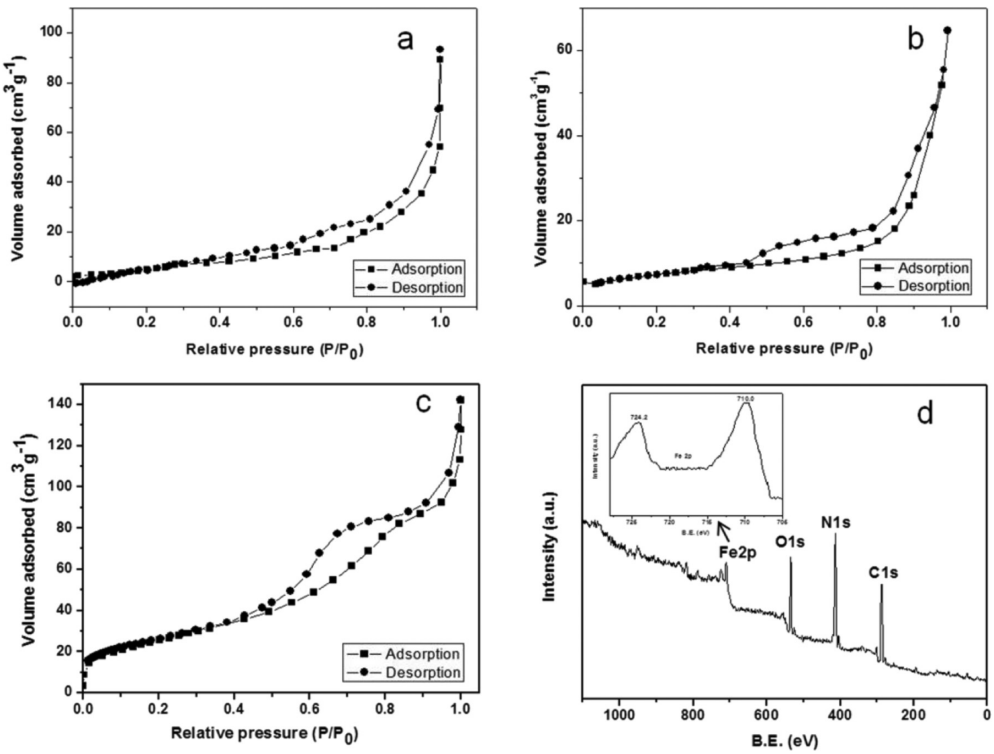

Figure 7. (a–c) Nitrogen adsorption–desorption isotherm plots for (a) pure Fe_3O_4, (b) pure g-C_3N_4, and (c) the as-prepared g-C_3N_4–Fe_3O_4 photocatalysts. (d) XPS spectrum of CNFO-15.2. The inset shows the high-resolution Fe 2p spectrum.

dx.doi.org/10.1021/jp409651g | J. Phys. Chem. C 2013, 117, 26135–26143

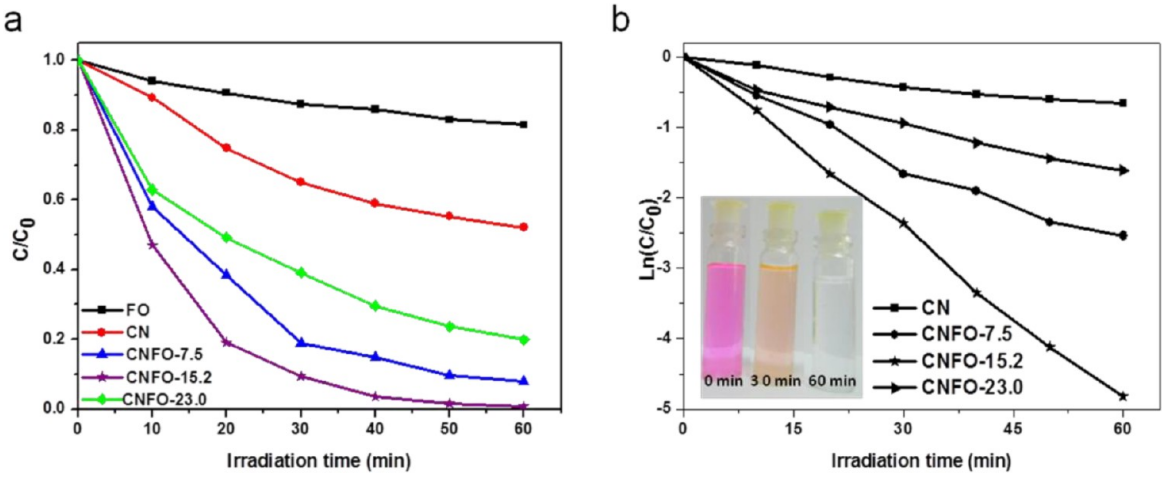

Figure 8. (a) Photocatalytic degradation of RhB over pure g-C_3N_4, pure Fe_3O_4, and the as-prepared g-C_3N_4–Fe_3O_4 photocatalysts under visible-light irradiation. (b) Plots of $\ln(C/C_0)$ vs time. The inset is a photograph showing the degradation of RhB over the g-C_3N_4–Fe_3O_4 photocatalyst.

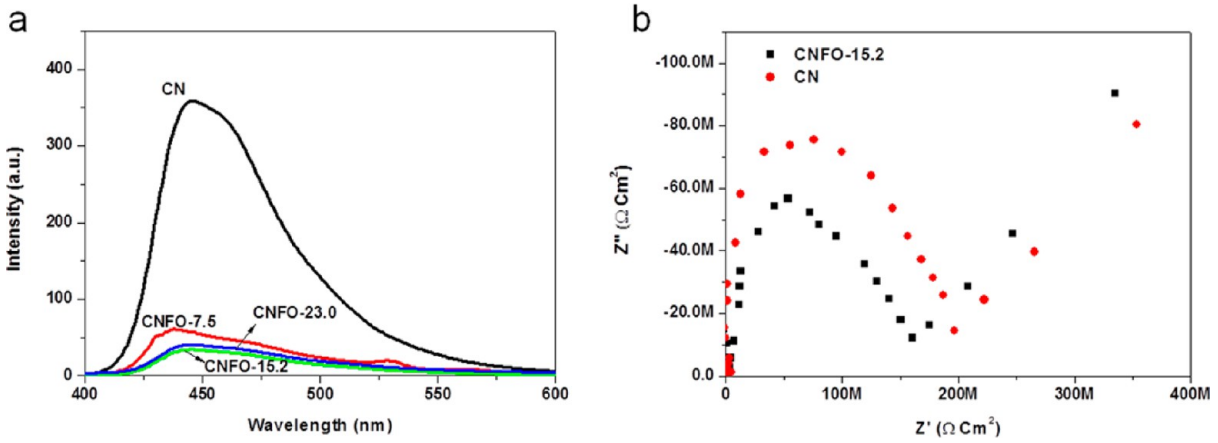

Figure 9. (a) PL spectra of pure g-C_3N_4, Fe_3O_4, and the as-prepared g-C_3N_4–Fe_3O_4 photocatalysts at an excitation wavelength of 365 nm at room temperature. (b) EIS profiles of CN and CNFO-15.2.

before the photodegradation test. As shown in Figure S3 in the Supporting Information, the g-C_3N_4–Fe_3O_4 nanocomposite exhibited a much higher RhB adsorption capacity than pure g-C_3N_4. The results indicated that the presence of the catalyst and light is essential for the efficient degradation of RhB under visible-light irradiation. As shown in Figure 8b, the plots of $\ln(C/C_0)$ versus irradiation time were linear, which indicates that the photodegradation of the RhB went through a pseudo-first-order kinetic reaction.[31] The optimum photocatalytic activity of g-C_3N_4–Fe_3O_4 at an Fe_3O_4 mass content of 15.2% under visible-light irradiation is almost 7 times higher than that of pure g-C_3N_4. The enhanced photocatalytic performance of the g-C_3N_4–Fe_3O_4 nanocomposite may be attributed to the synergistic effect between the interface of Fe_3O_4 and g-C_3N_4.

3.4. Photoluminescence. In order to disclose the effect of Fe_3O_4 modification, PL spectral analysis was carried out to reveal the migration, transfer, and recombination processes of photoinduced electron–hole pairs in the composite system. Figure 9a shows the PL spectra of pure g-C_3N_4 and the g-C_3N_4–Fe_3O_4 nanocomposites with an excitation wavelength of 365 nm at room temperature. As can be seen in Figure 9a, the main emission peak is centered at about 435 nm for the pure g-C_3N_4 sample. The PL intensity of the g-C_3N_4–Fe_3O_4 nanocomposites is significantly decreased, which indicates that the composite has a much lower recombination rate of photoinduced electron–hole pairs.[19]

3.5. EIS. In addition, EIS measurements were conducted to investigate the charge transfer resistance and the separation efficiency of the photoinduced charge carriers. As can be seen from Figure 9b, the diameter of the Nyquist semicircle for CNFO-15.2 nanocomposite is smaller than those of g-C_3N_4 and Fe_3O_4 (not shown), which indicates that the CNFO-15.2 nanocomposite has a lower resistance than g-C_3N_4 and Fe_3O_4. This result demonstrates that the introduction of Fe_3O_4 into g-C_3N_4 can enhance the separation and transfer efficiency of photoinduced electron–hole pairs,[20] which is a favorable condition for improving the photocatalytic activity.

3.6. Reusability. To study the stability of the as-prepared g-C_3N_4–Fe_3O_4 photocatalyst, the used g-C_3N_4–Fe_3O_4 was collected, and the reusability was further examined in six successive RhB degradation experiments. As shown in Figure 10, g-C_3N_4–Fe_3O_4 retained over 90% of its original photocatalytic activity after six successive experimental runs, which is also very important from a practical application point of view. The PXRD pattern of the g-C_3N_4–Fe_3O_4 composite after six successive experimental runs is presented in Figure S4 in the Supporting Information. It can be seen that no new peak appeared in the composite system. Therefore, the g-C_3N_4–

dx.doi.org/10.1021/jp409651g | J. Phys. Chem. C 2013, 117, 26135–26143

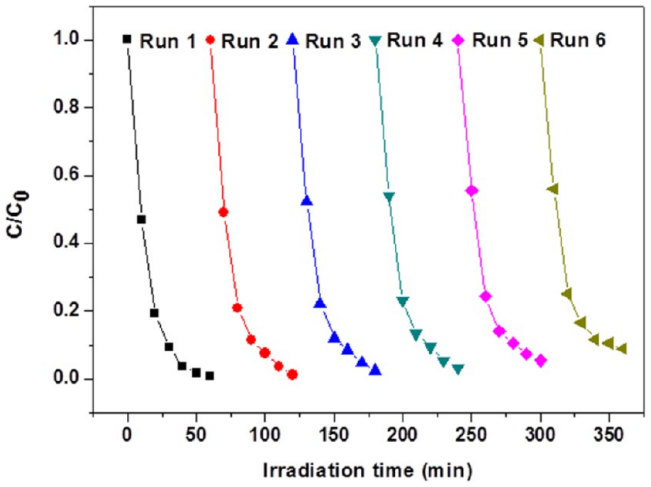

Figure 10. Recyclability of the g-C_3N_4–Fe_3O_4 photocatalyst for the degradation of RhB under visible-light irradiation.

Fe_3O_4 composite can be used efficiently in environmental protection.

3.7. Magnetic Properties (Separation of the g-C_3N_4–Fe_3O_4 Hybrid Nanocomposite after the Reaction). To collect and reuse the photocatalyst in multiple cycles, its preparation with good superparamagnetism is essential. Figure 11 shows images of the behavior of the g-C_3N_4–Fe_3O_4 hybrid

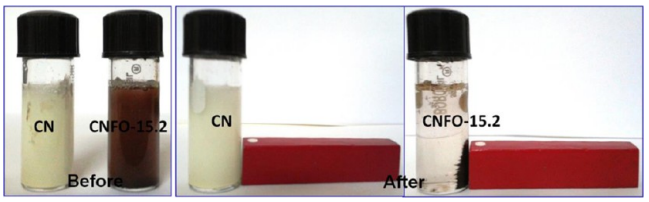

Figure 11. Images showing the separation of the g-C_3N_4–Fe_3O_4 photocatalyst dispersed in water using a permanent magnet to provide an external magnetic field.

nanocomposite dispersed in water in a magnetic field under neutral conditions. As can be seen from Figure 11, the g-C_3N_4–Fe_3O_4 photocatalyst is strongly attracted to a permanent magnet. Therefore, the g-C_3N_4–Fe_3O_4 photocatalysts can be rapidly separated under an applied magnetic field.

3.8. Detection of Reactive Oxidative Species. In general, reactive species including $^{\bullet}OH$ and $O_2^{\bullet-}$ are expected to be involved in the photocatalytic process. To investigate the role of these reactive species in the g-C_3N_4–Fe_3O_4 system, the effects of some radical scavengers and N_2 purging on the photodegradation of RhB were studied. It can be seen from Figure 12a that when N_2 purging was conducted as an $O_2^{\bullet-}$ scavenger, a dramatic change in the photocatalytic activity was observed compared with the absence of scavenger, confirming that the dissolved O_2 has a clear effect on the photodegradation process under visible-light irradiation. Meanwhile, a similar change in the photocatalytic activity was observed upon the addition of tBuOH as an OH scavenger. However, no change in the photocatalytic activity was observed upon the addition of ammonium oxalate (AO) as a hole scavenger compared with no scavenger under similar conditions, indicating that the $O_2^{\bullet-}$ and $^{\bullet}OH$ are the main reactive species in the g-C_3N_4–Fe_3O_4 system. Moreover, PL spectra were used to disclose the formation of $^{\bullet}OH$. As can be seen in Figure 12b, the PL emission peak of 2-hydroxyterephthalic acid was observed and gradually increased with the irradiation time, which indicates the formation of photoinduced $^{\bullet}OH$ under visible-light irradiation.

3.9. Mechanism of Enhanced Photocatalytic Performance. A schematic drawing illustrating the synergistic effect in the photocatalytic degradation of RhB over the g-C_3N_4–Fe_3O_4 hybrid composite is shown in Figure 13. Under visible-light irradiation, the photoinduced electrons can easily be transferred from the conduction band (CB) of g-C_3N_4 to the CB of Fe_3O_4 because the CB level of Fe_3O_4 is lower than that of g-C_3N_4 (i.e., energy matching band structure is observed in the g-C_3N_4–Fe_3O_4 hybrid composite system).[9,30] Furthermore, because of the high conductivity of Fe_3O_4, the rate of electron transport is fast, which suppresses the direct recombination of photoinduced electron–hole pairs in the g-C_3N_4–Fe_3O_4 hybrid composite system. Thus, Fe_3O_4 acts as an acceptor of the photoinduced electrons from g-C_3N_4. Therefore, because of the presence of the g-C_3N_4–Fe_3O_4 interface, the chance of recombination of photoinduced electron–hole pairs is further successfully suppressed, leaving more charge carriers to form reactive species. The electrons in the CB of Fe_3O_4 are good

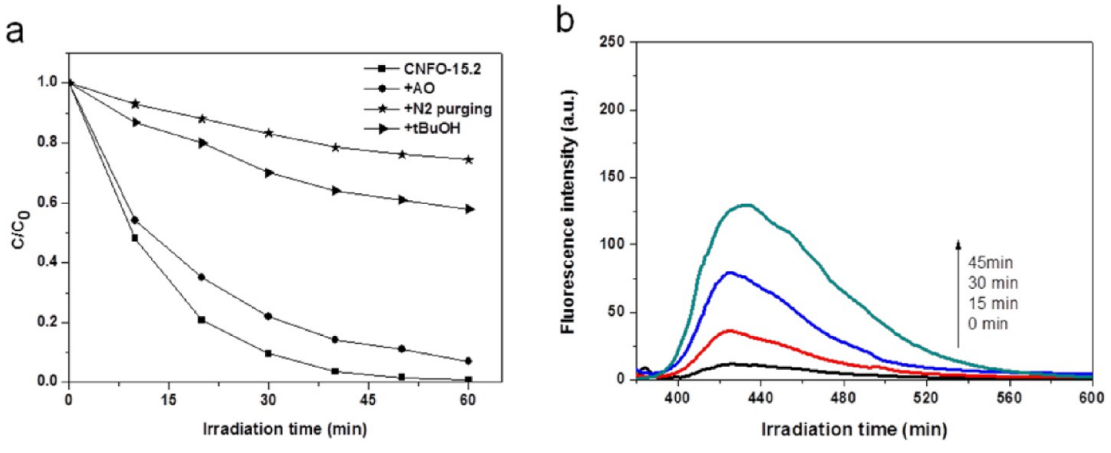

Figure 12. (a) Effects of different scavengers on the degradation of RhB in the presence of the g-C_3N_4–Fe_3O_4 photocatalyst under visible-light irradiation. (b) $^{\bullet}OH$ trapping PL spectra of the g-C_3N_4–Fe_3O_4 photocatalyst with TA solution under visible-light irradiation.

dx.doi.org/10.1021/jp409651g | J. Phys. Chem. C 2013, 117, 26135–26143

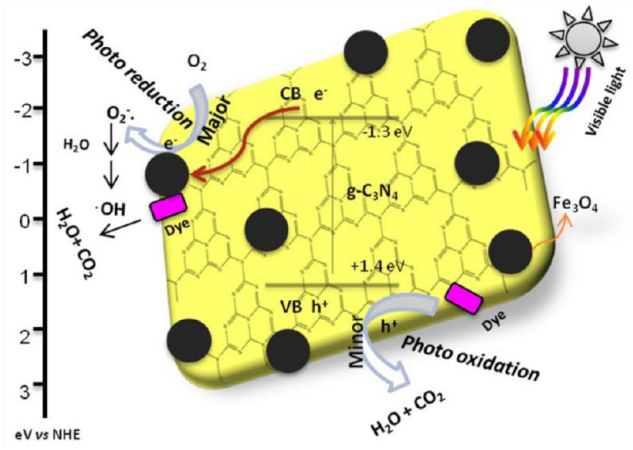

Figure 13. Schematic illustration of the mechanism for photoinduced charge carrier transfers in the g-C_3N_4–Fe_3O_4 photocatalyst under visible-light irradiation.

reductants that could efficiently reduce the O_2 adsorbed onto the composite catalyst surface into various reactive speices ($O_2^{\bullet-}$, $HO_2^{\bullet}$, H_2O_2), subsequently leading to the formation of $^{\bullet}OH$ and oxidation of RhB into CO_2, H_2O, etc. Therefore, the enhanced photocatalytic activity is achieved.

4. CONCLUSION

In summary, g-C_3N_4–Fe_3O_4 nanocomposites have been successfully and directly prepared by a facile, effective, and reproducible in situ growth mechanism. Monodispersed Fe_3O_4 nanoparticles with a size of about 8 nm are uniformly deposited on the g-C_3N_4 sheets, which effectively prevents the Fe_3O_4 nanoparticles from aggregating together. The g-C_3N_4–Fe_3O_4 nanocomposite exhibits enhanced photocatalytic activity for the degradation of RhB under visible-light irradiation. More importantly, g-C_3N_4–Fe_3O_4 photocatalyst could be recovered by an applied magnetic field and reused without loss of photocatalytic activity even after six successive cycles. Therefore, the g-C_3N_4–Fe_3O_4 nanocomposite is a promising photocatalytic material for environmental applications as well as water splitting.

■ ASSOCIATED CONTENT

Supporting Information

Flowchart for preparation of g-C_3N_4–Fe_3O_4, TEM images of the as-prepared CNFO-7.2 and CNFO-23.0, adsorption ability of the as-prepared CN and CNFO-15.2 photocatalysts, and XRD pattern of the reused CNFO-15.2 photocatalyst. This material is available free of charge via the Internet at http://pubs.acs.org.

■ AUTHOR INFORMATION

Corresponding Author

*Tel.: +91-870-2462675. Fax: +91-870-2459547. E-mail: vishnu@nitw.ac.in.

Notes

The authors declare no competing financial interest.

■ ACKNOWLEDGMENTS

Authors thank DST, Government of India, for financial support (SR/FT/CS-096/2009). S.K. also thanks MHRD, Government of India, for providing a fellowship.

■ REFERENCES

(1) Hoffmann, M. R.; Martin, S. T.; Choi, W.; Bahnemann, D. W. Environmental Applications of Semiconductor Photocatalysis. *Chem. Rev.* **1995**, *95*, 69–96.
(2) Chen, X.; Shen, S.; Guo, L.; Mao, S. S. Semiconductor-Based Photocatalytic Hydrogen Generation. *Chem. Rev.* **2010**, *110*, 6503–6570.
(3) Rajeshwar, K.; Osugi, M. E.; Chanmanee, W.; Chenthamarakshan, C. R.; Zanoni, M. V. B.; Kajitvichyanukul, P.; Krishnan-Ayer, R. Heterogeneous Photocatalytic Treatment of Organic Dyes in Air and Aqueous Media. *J. Photochem. Photobiol., C* **2008**, *9*, 171–192.
(4) Prashant, V. K. Meeting the Clean Energy Demand: Nanostructure Architectures for Solar Energy Conversion. *J. Phys. Chem. C* **2007**, *111*, 2834–2860.
(5) Mohamed, R. M.; McKinney, D. L.; Sigmund, W. M. Enhanced Nanocatalysts. *Mater. Sci. Eng.* **2012**, *73*, 1–13.
(6) Rehman, S.; Ullah, R.; Butt, A. M.; Gohar, N. D. Strategies of Making TiO_2 and ZnO Visible Light Active. *J. Haz. Mater.* **2009**, *170*, 560–569.
(7) Yi, Z.; Ye, J.; Kikugawa, N.; Kako, T.; Ouyang, S.; Stuart-Williams, H.; Yang, H.; Cao, J.; Luo, W.; Li, Z.; Liu, Y.; Withers, R. L. An Orthophosphate Semiconductor with Photooxidation Properties under Visible-Light Irradiation. *Nat. Mater.* **2010**, *9*, 559–564.
(8) Li, Y.; Wang, J.; Yao, H.; Dang, L.; Li, Z. Efficient Decomposition of Organic Compounds and Reaction Mechanism with BiOI Photocatalyst under Visible Light Irradiation. *J. Mol. Catal. A: Chem.* **2011**, *334*, 116–122.
(9) Wang, X.; Maeda, K.; Thomas, A.; Takanabe, K.; Xin, G.; Carlsson, J. M.; Domen, K.; Antonietti, M. A Metal-Free Polymeric Photocatalyst for Hydrogen Production from Water under Visible Light. *Nat. Mater.* **2009**, *8*, 76–80.
(10) Zhang, Y.; Mori, T.; Ye, J. Polymeric Carbon Nitrides: Semiconducting Properties and Emerging Applications in Photocatalysis and Photoelectrochemical Energy Conversion. *Sci. Adv. Mater.* **2012**, *4*, 282–291.
(11) Zhou, X.; Jin, B.; Chen, R.; Feng, P.; Fang, Y. Synthesis of Porous Fe_3O_4/g-C_3N_4 Nanospheres as Highly Efficient and Recyclable Photocatalysts. *Mater. Res. Bull.* **2013**, *48*, 1447–1452.
(12) Pan, C.; Xu, J.; Wang, Y.; Li, D.; Zhu, Y. Dramatic Activity of C_3N_4/$BiPO_4$ Photocatalyst with Core/Shell Structure Formed by Self-Assembly. *Adv. Funct. Mater.* **2012**, *22*, 1518–1524.
(13) Wang, X.; Blechert, S.; Antonietti, M. Polymeric Graphitic Carbon Nitride for Heterogeneous Photocatalysis. *ACS Catal.* **2012**, *2*, 1596–1606.
(14) Wang, Y.; Shi, R.; Lin, J.; Zhu, Y. Enhancement of Photocurrent and Photocatalytic Activity of ZnO Hybridized with Graphite-like C_3N_4. *Energy Environ. Sci.* **2011**, *4*, 2922–2929.
(15) Ge, L.; Han, C.; Liu, J.; Li, Y. Enhanced Visible Light Photocatalytic Activity of Novel Polymeric g-C_3N_4 loaded with Ag Nanoparticles. *Appl. Catal., A* **2011**, *409–410*, 215–222.
(16) Yan, S. C.; Li, Z. S.; Zou, Z. G. Photodegradation of Rhodamine B and Methyl Orange over Boron-Doped g-C_3N_4 under Visible Light Irradiation. *Langmuir* **2010**, *26*, 3894–3901.
(17) Dong, G.; Zhao, K.; Zhang, L. Carbon Self-Doping Induced High Electronic Conductivity and Photoreactivity of g-C_3N_4. *Chem. Commun.* **2012**, *48*, 6178–6180.
(18) Ge, L.; Han, C.; Xiao, X.; Guo, L.; Li, Y. Enhanced Visible Light Photocatalytic Hydrogen Evolution of Sulfur-Doped Polymeric g-C_3N_4 Photocatalysts. *Mater. Res. Bull.* **2013**, *48*, 3919–3925.
(19) Kumar, S.; Surendar, T.; Baruah, A.; Shanker, V. Synthesis of A Novel and Stable g-C_3N_4–Ag_3PO_4 Hybrid Nanocomposite Photocatalyst and Study of the Photocatalytic Activity under Visible Light Irradiation. *J. Mater. Chem. A* **2013**, *1*, 5333–5340.
(20) Huang, L.; Xu, H.; Li, Y.; Li, H.; Cheng, X.; Xi, J.; Xu, Y.; Cai, G. Visible-Light-Induced WO_3/g-C_3N_4 Composites with Enhanced Photocatalytic Activity. *Dalton Trans* **2013**, *42*, 8606–8616.

(21) Lu, X.; Wang, Q.; Cui, D. Preparation and Photocatalytic Properties of g-C_3N_4/TiO_2 Hybrid Composite. *J. Mater. Sci. Technol.* **2010**, *26*, 925−930.
(22) He, Y.; Cai, J.; Li, T.; Wub, Y.; Lin, H.; Zhao, L.; Luo, M. Efficient Degradation of RhB Over $GdVO_4$/g-C_3N_4 Composites under Visible Light Irradiation. *Chem. Eng. J.* **2013**, *215*−*216*, 721−730.
(23) Li, X.; Huang, X.; Liu, D.; Wang, X.; Song, S.; Zhou, L.; Zhang, H. Synthesis of 3D Hierarchical Fe_3O_4/Graphene Composites with High Lithium Storage Capacity and for Controlled Drug Delivery. *J. Phys. Chem. C* **2011**, *115*, 21567−21573.
(24) Yang, X.; Zhang, X.; Ma, Y.; Huang, Y.; Wang, Y.; Chen, Y. Superparamagnetic Graphene Oxide−Fe_3O_4 Nanoparticles Hybrid for Controlled Targeted Drug Carriers. *J. Mater. Chem.* **2009**, *19*, 2710−2714.
(25) Jing, S.; Cao, M.; Ren, L.; Hu, C. Fe_3O_4/Graphene Nanocomposites with Improved Lithium Storage and Magnetism Properties. *J. Phys. Chem. C* **2011**, *115*, 14469−14477.
(26) Xu, P.; Zeng, G. M.; Huang, D. L.; Feng, C. L.; Shuang, H.; Zhao, M. H.; Lai, C.; Zhen, W.; Huang, C.; Xie, G. X.; Liu, Z. F. Use of Iron Oxide Nanomaterials in Wastewater Treatment: A Review. *Sci. Total Environ.* **2012**, *424*, 1−10.
(27) Chen, W. J.; Tsai, P. J.; Chen, Y. C. Functional Fe_3O_4/TiO_2 Core/Shell Magnetic Nanoparticles as Photokilling Agents for Pathogenic Bacteria. *Small* **2008**, *4*, 485−491.
(28) Xie, J.; Chen, K.; Lee, H. Y.; Xu, C.; Hsu, A. R.; Peng, S.; Chen, X.; Sun, S. Ultrasmall c(RGDyK)-Coated Fe_3O_4 Nanoparticles and Their Specific Targeting to Integrin rv3-Rich Tumor Cells. *J. Am. Chem. Soc.* **2008**, *130*, 7542−7543.
(29) Ren, L.; Huang, S.; Fan, W.; Liu, T. One-Step Preparation of Hierarchical Superparamagnetic Iron Oxide/Graphene Composites Via Hydrothermal Method. *Appl. Surf. Sci.* **2011**, *258*, 1132−1138.
(30) Xi, G.; Yue, B.; Cao, J.; Ye, J. Fe_3O_4/WO_3 Hierarchical Core−Shell Structure: High-Performance and Recyclable Visible-Light Photocatalysis. *Chem.—Eur. J.* **2011**, *17*, 5145−5154.
(31) Chalasani, R.; Vasudevan, S. Cyclodextrin-Functionalized Fe_3O_4@TiO_2: Reusable, Magnetic Nanoparticles for Photocatalytic Degradation of Endocrine-Disrupting Chemicals in Water Supplies. *ACS Nano* **2013**, *7*, 4093−4104.
(32) Liang, H.; Niu, H.; Li, P.; Tao, Z.; Mao, C.; Song, J.; Zhang, S. Multifunctional Fe_3O_4@C@Ag Hybrid Nanoparticles: Aqueous Solution Preparation, Characterization and Photocatalytic Activity. *Mater. Res. Bull.* **2013**, *48*, 2415−2419.
(33) Xuan, S.; Jiang, W.; Gong, X.; Hu, Y.; Chen, Z. Magnetically Separable Fe_3O_4/TiO_2 Hollow Spheres: Fabrication and Photocatalytic Activity. *J. Phys. Chem. C* **2009**, *113*, 553−558.